2015

Angular Dependence of the Emission from the Intrinsic Josephson Junction in Pie-Shaped Wedge Triangular BSCCO Mesas

Manuel Morales
University of Central Florida

ANGULAR DEPENDENCE OF THE EMISSION FROM THE INTRINSIC JOSEPHSON JUNCTION IN PIE-SHAPED WEDGE TRIANGULAR BSCCO MESAS

by

MANUEL MORALES

A thesis submitted in partial fulfillment of the requirements
for the Honors in the Major Program in Physics
in the College of Science
and in The Burnett Honors College
at the University of Central Florida
Orlando, Florida

Spring Term 2015

Thesis Chair: Dr. Richard Klemm

ABSTRACT

The purpose of this thesis is to determine the radiation patterns from an acute isosceles triangular superconducting mesa modeled by a pie-shaped geometry.

The terahertz band lies between the microwave and infrared regions of the electromagnetic spectrum. The terahertz radiation from atomic-scale layered superconducting mesas is caused by the tunneling of electron pairs in the ac-Josephson effect. To determine the terahertz power radiated per unit solid angle of an acute isosceles triangular superconducting mesa, a model was employed in which the shape of the mesa is approximated as a pie-shaped wedge. This model is shown to have an accuracy of about 1%. Using Love's Equivalency Principle, the current caused by the Josephson effect is then assumed to be on the edges of the mesa.

Since in the mesas used for experiments the electric field is in the direction of the current, it is parallel to the boundary of the sample. Hence, we want the TM modes, and that requires the magnetic field to be transverse to the boundary. We thus require that the tangential component of the magnetic field parallel at the boundary vanishes. Love's equivalency principle provides the easiest and most straight forward way to satisfy this condition.

The surface electric current density was modeled by comparing the magnetic vector potential resulting from the modeled edge current with that given by a standard volume average integration technique. The surface current density that provided the best approximation to the bulk average was used and the radiation patterns were plotted using Mathematica software.

DEDICATION

To my family

ACKNOWLEDGMENTS

First and foremost, I would like to thank my adviser Dr. Richard Klemm for not only giving me the opportunity to work on this exciting research field but also for being an exemplary model to follow. Dr. Klemm's relentless motivation and work ethic have truly set a standard which I will use to guide my future endeavors.

I would also like to acknowledge William Stillwell for being an exceptional mentor throughout my first undergraduate years of school. I also want to thank Dr. Helge Heinrich and Dr. Lee Chow for being exemplary professors and for sharing their academic wisdom and insights.

Finally, I want to thank my friends James Westley and Tyler Fletcher for their support and friendship.

TABLE OF CONTENTS

LIST OF FIGURES

LIST OF TABLES

CHAPTER 1: INTRODUCTION

The terahertz (THz) band lies between the microwave and infrared regions of the electromagnetic spectrum. Roughly defined, the THz spectral region lies between 0.1 and 10 THz. This corresponds to an energy between 0.4 meV and 40 meV with a wavelength between 3 mm and 30 μm. The THz region was commonly referred to as the terahertz gap, given that few compact continuous wave (CW) sources capable of producing radiation in this regime exist and generating THz radiation at any meaningful power levels presents many practical hurdles, particulary in the region between 1 and 2 THz.

Electromagnetic radiation in the THz frequency domain has unique properties that make it particularly attractive for research in ultra-high speed communications, quantum information, pharmaceutical industries, medicine and medical diagnoses, bio-sciences and biotechnologies, non-destructive sensing and testing, and various kinds of imaging purposes [Delfanazari et al., 2013].

THz electromagnetic waves are particularly well suited for the study of biological organisms, making it an attractive source of radiation in medical applications such as epithelial cancer detection. A thorough understanding of the radiation patterns is essential for the development of imaging tools such as hand-held cancer detection probes among others.

In recent years, a number of methods for generating both CW and pulsed THz radiation have been successfully developed. At present, THz sources such as Quantum Cascade lasers, Resonance Tunneling Diodes, Gunn Diodes, Backward Wave Oscillators, and Super-Lattice Electronic Devices are not only large, expensive, and cumbersome devices but also usually provide limited power at THz frequencies. Furthermore, for most compact sources, as the frequency increases the output power plummets by the relation $Pf^2 = constant$, where P is the power generated and f is the frequency of the source [Armstrong, 2012]. Furthermore, CW devices that offer a viable power levels

often lack the tunable capabilities required to perform THz-Time-Domain Spectroscopy which uses coherent detection to record both the amplitude and the phase of the THz wave.

In has been suggested [Delfanazari et al., 2013] that the ac-Josephson effect intrinsic to an atomic-scale layered superconductor may provide a source that is both compact and able to generate intense THz EM waves. The THz radiation from atomic-scale layered superconducting mesas is caused by the tunneling of electron pairs in the ac-Josephson effect, and the radiation from layered mesas has been found to be coherent with a power that behaves as N^2, where N is the number of intrinsic Josephson junctions (IJJs). This behavior suggests the possibility of enhancing the emission power by the synchronization of arrays [Orita et al., 2010].

This study will focus on tunable THz emission from the IJJs in pie-shaped wedge BSCCO mesas as it has been shown that triangular geometries are promising candidates for synchronization purposes in particular because their circular polarization features are important to array design [Bahl and Bhartiya, 1980]. The expected radiation pattern from acute isosceles triangular mesas has not yet been published [Delfanazari et al., 2013], therefore the primary focus of this study will be to approximate the angular dependence of an acute isosceles mesa with a pie-shaped wedge to fit and plot the radiation patterns observed in these mesas.

A Brief History of Terahertz Emissions

Before gaining strong popularity, the THz band went by names such as near millimeter, sub-millimeter, and extreme far infrared. In the 1950s, early interest in this band was sought after by molecular spectroscopists. In the 1970s, space scientists used infrared and sub-millimeter wave spectrometers to investigate the chemical compositions of interstellar medium and planetary atmospheres [Armstrong, 2012]. More recently, the unique properties of THz radiation have sparked

significant interest in the field of medical physics, more specifically in the areas of imaging and sensing.

Superconductivity and the Josephson Effect

Figure 1.1: Brian D. Josephson

Superconductivity was discovered in 1911 by H. Kamerlingh Onnes in Leiden, just three years after he had first liquefied helium [Tinkham, 1975]. Superconductivity is a phenomenon in which exactly zero electrical resistance occurs in certain materials when cooled below a characteristic critical temperature T_c. In 1962, B. D. Josephson introduced to the world of superconductivity his tunneling theory; he proposed that a tunnel junction should show a zero voltage supercurrent due to the tunneling of condensed pairs [Tinkham, 1975]. The tunneling of electrons is not, however, a property of superconductivy. If two metals are separated by a very thin strip of insulating material, electrons can tunnel mechanically from one into the other, and a current can pass through the junction. For normal metals the resulting resistance is ohmic, but if the metals are superconductive the resistance is not ohmic and indeed the resulting resistance can provide information about the superconductor [Decker, 1969]. Josephson further predicted that, if a voltage difference V_{jct} were maintained across the junction, the current would be an alternating current [Tinkham, 1975].

One may develop an intuitive understanding by using the following simple model: As pictured in figure 1.2a, when the electron pairs tunnel through the Josephson junction they experience an energy change of $2eV_{\text{jct}}$. Without dissipation, this energy must go somewhere else for this process to be reversible. This energy is then emitted as a photon of energy $h\nu = 2eV_{\text{jct}}$.

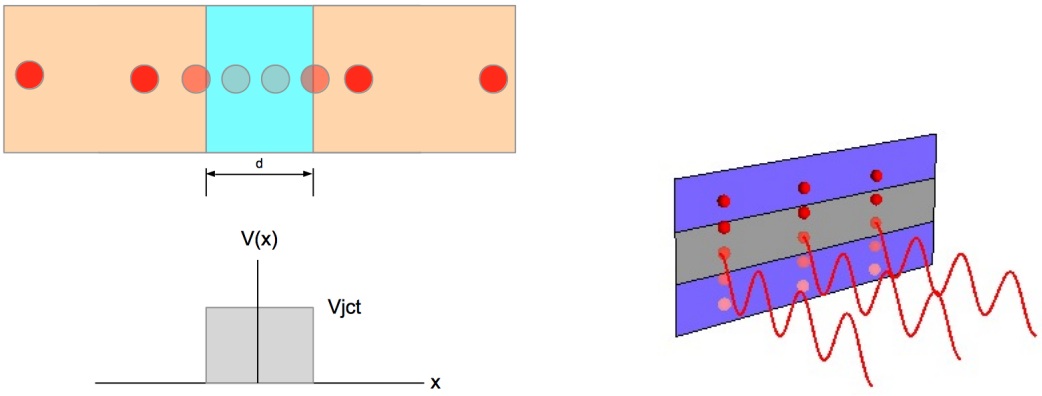

(a) (b)

Figure 1.2: A simplified model of the ac Josephson effect for (a) one junction and (b) multiple junctions.

As picture in figure 1.2b, electron pairs oscillate back and forth with frequency $\nu_J = 2eV_{\text{jct}}/h$, known as the Josephson frequency. For N synchronized junctions, each junction tunnels with a frequency $\nu_J = \frac{2e}{h}\frac{V_0}{N}$, where $V_{\text{jct}} = V_0/N$ is the potential across each junction and V_0 is the total voltage across the sample. Each junction can have a large number of harmonics at $\nu_n = n\nu_J$, therefore we may conclude that the ac Josephson current is of the form $J_n^J e^{-in\omega_J t}$, where J_n^J is the amplitude of oscillation and $\omega_J = 2\pi\nu_J$.

We want to develop, however, a better understanding of the ac Josephson effect in order to better understand the nature of the radiation observed in BSCCO. Pictured in figure 1.3 is a model of a Josephson junction. The junction (top) is composed of two superconducting layers separated by an insulating layer of thickness d. A constant potential V_{jct} is placed across the junction and the wavefunction along the junction can be taken as $\psi = |\psi|e^{i\phi}$.

As given by elementary quantum mechanics, in the absence of electromagnetic fields, the current

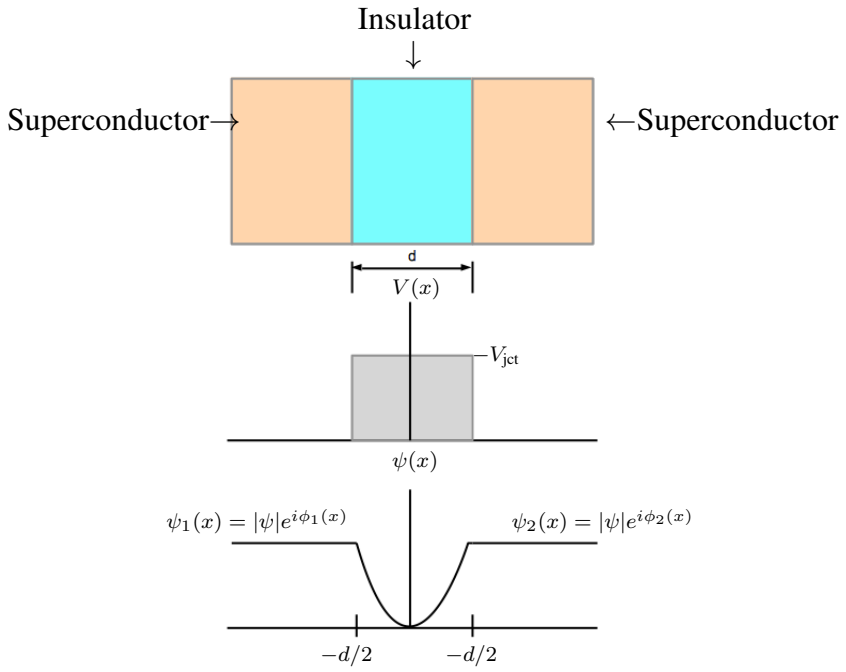

Figure 1.3: A more sophisticated model of the ac Josephson effect.

density created by the wave function is given by:

$$J(x,t) = ei(x,t) = \frac{e}{2m}(\psi\hat{p}_x^*\psi^* + \psi^*\hat{p}_x\psi)),$$

where $J(x,t)$ is the electric current density, $i(x,t)$ is the probability current density, and $\hat{p}_x$ is the momentum operator given by $\hat{p}_x = -i\hbar\frac{d}{dx}$. Thus, the current density for the cases where there is no potential is given by

$$J(x) = \frac{e\hbar}{m}|\psi|^2\frac{d\phi(x)}{dx}$$

In the presence of electromagnetic fields, the *generalized* momentum operator is given by:

$$\hat{p}_x \longrightarrow \hat{p}_x - \frac{e}{c}\hat{A}_x$$

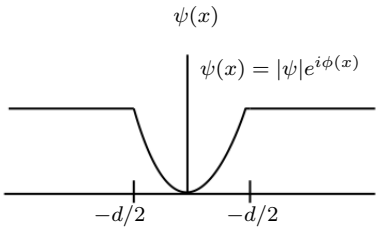

Figure 1.4: The wave function in the tunneling region.

Therefore the corresponding equation for the supercurrent is modified such that

$$J_S(x,t) = \frac{2e\hbar}{m}|\psi|^2\Big(\frac{d\phi(x)}{dx} - \frac{2\pi}{\Phi_0}\hat{A}_x\Big),$$

where the factor of 2 reflects the fact that electrons tunnel in pairs and the quantum flux is defined by $\Phi_0 = \frac{hc}{2e}$. Integrating both sides of this equation and assuming J_S and $|\psi|^2$ are constant through the thickness d we obtain:

$$J_S = J^J\gamma,$$

where $J^J = \frac{2e\hbar}{md}$ and the gauge-invariant phase difference is given by

$$\gamma = (\phi_2 - \phi_1) - \frac{2\pi}{\Phi_0}\int_{-d/2}^{d/2} A_x dx$$

We may also replace the supercurrent such that [Tinkham, 1975]:

$$J_s = J^J \sin\gamma$$

For time dependent potentials it can also be shown that γ satisfies

$$\frac{\partial\gamma(x,t)}{\partial t} = \frac{2\pi}{\Phi_0}\int_{-d/2}^{d/2} E(x,t)dx$$

For a constant potential V_{jct} across d:

$$\frac{\partial\gamma(x,t)}{\partial t} = \frac{2\pi}{\Phi_0}\int_{-d/2}^{d/2} E(x,t)dx = \frac{2\pi}{\Phi_0}V_{\text{jct}},$$

therefore

$$J_s = J^J \sin\left[\gamma(0) + \frac{2\pi}{\Phi_0}V_{\text{jct}}t\right] = J^J \sin\left[\gamma(0) + \nu_J t\right],$$

where $\nu_J = \frac{2\pi}{\Phi_0}V_{\text{jct}} = \frac{2e}{\hbar}V_{\text{jct}}$ is the Josephson frequency and J_s is an oscillating current. This agrees with the result obtained from the simplified model and we now know the value of J^J.

BSCCO

Generally speaking, a *mesa* is an elevated area of land with a flat top, surrounded on all sides by steep cliffs. In this context, a *superconducting mesa* has a structure with a shape similar to these geological formations. Bismuth strontium calcium copper oxide, or BSCCO is a family of high temperature superconductors that can be used as a source of THz radiation. BSCCO may be described by its general formula $Bi_2Sr_2Ca_{n-1}Cu_nO_{2n+4+\delta}$. The $n = 2$ compound $Bi_2Sr_2CaCu_2O_{8+\delta}$ is sometimes also referred to as $\text{Bi}-2212$. In this thesis we will use the name BSCCO whenever referencing the sample. A molecular view of the BSCCO compound is pictured in Fig. 1.5

BSCCO behaves as a stack of intrinsic Josephson junctions (IJJs) with a superconducting layer (CuO) separated by an insulating layer (BiO and SrO). In BSCCO, each of the junctions is naturally identical, as they are evenly spaced with two junctions per unit cell. By applying a static (dc) voltage V_0 across the mesa, the ac Josephson effect is generated in each of the N junctions involved in the mesa, and coherent ac Josephson radiation at terahertz frequencies is emitted.

BSCCO can produce useful emission power if one can achieve the synchronization of the high-

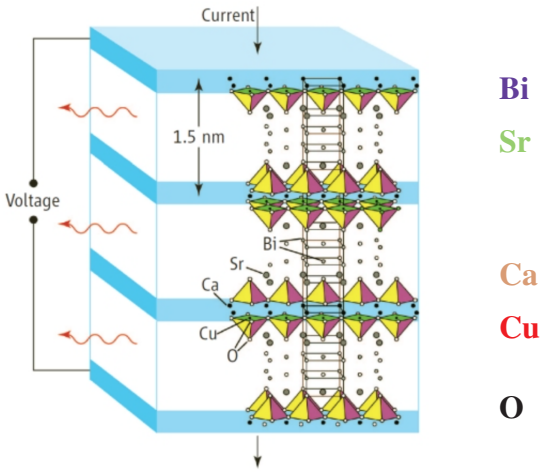

Figure 1.5: A simplified molecular view of BSCCO

frequency oscillations of all the junctions in the stack. Experiments by Ozyuzer et al. (2007) showed that emission from the junctions in BSCCO is synchronized by a standing electromagnetic wave that is formed by multiple reflections in the cavity formed by the side surfaces of the crystal, exactly as in a laser. Consider a rectangular mesa of length l, width w, and thickness h. Shown in figure 1.6 (left) is a two dimensional view of the width of the mesa. The junctions have a width of d and each junction experiences a potential difference V_{jct} when a voltage V_0 is placed across the sample.

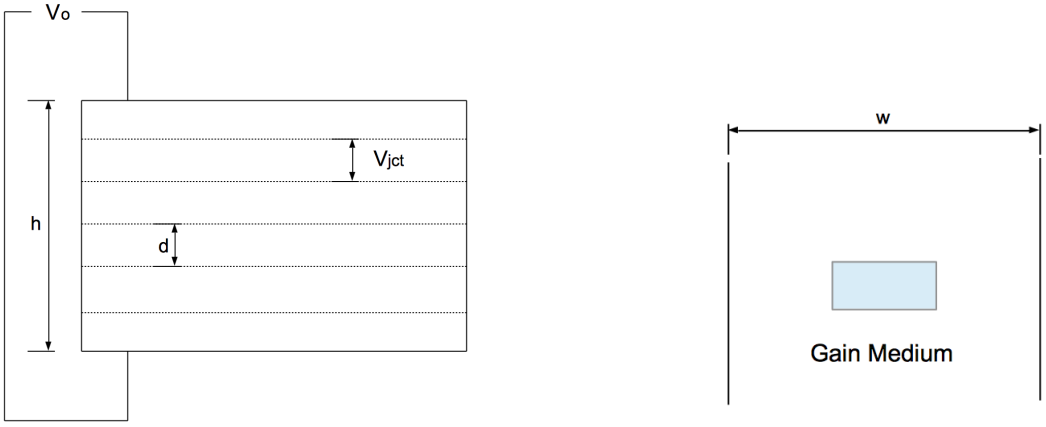

Figure 1.6: BSCCO laser model

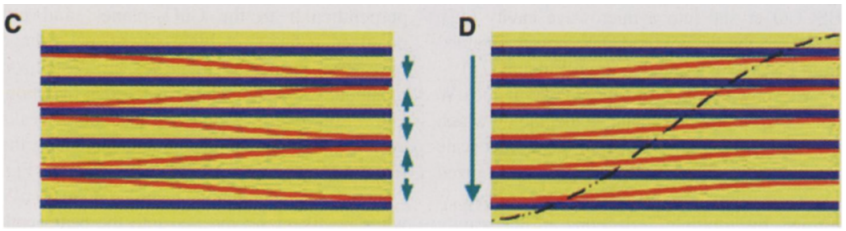

Figure 1.7: Schematic of the anti-phase (c) and the in-phase (d) modes[Ozyuzer, 2007].

Also pictured in figure 1.6 (right) is the laser model. In a laser, a gain medium may be capable of amplifying a certain range of frequencies. A cavity is formed by positioning a mirror on each side of the gain medium. Then, an electromagnetic field inside the cavity must satisfy the cavity boundary conditions, i.e. it must vanish at the boundaries. Thus, even though the gain medium is capable of amplifying a wide range of frequencies, only those frequencies which are supported by the cavity, or which satisfy the boundary conditions set by the cavity geometry, can be amplified. In particular, the fundamental (lowest) cavity mode (frequency) in a rectangular cavity of width w is $\nu = c/2n_r w$, where n_r is the index of refraction.

In analogy, the BSCCO mesa can be thought of as a gain medium which we can control by varying the voltage across the frequency to control which frequencies are amplified, and the cavity is formed by the sides of the mesa. Pictured in 1.7d, the in-phase mode coherent superposition of the electromagnetic waves (red curves) from each junction form a macroscopic coherent state (black curve) in which the radiation power increases as the square of the number of junctions. In figure 1.7c, due to complicated plasma resonances that occur along the long dimension of the mesa, the emission output from the long side of the mesa is not meaningful. Some of the values used in the experiments by Ozyuzer et al. (2007) are the following: *From the ac Josephson effect* - $h = 1.1\mu$m, $d = 1.56$ nm$\longrightarrow$ N =705, V_0 =0.71 V, $V_{\text{jct}} = V_0/N$ =1.01 mV, ν_J =483.6$\times$ V_{jct} THz= 0.49 THz. *From the cavity mode* - w=80 μm, $n_r \approx 3.5 \longrightarrow \nu = c/2n_r w = 0.52$ THz. *Experimental results* - ν=0.48 THz

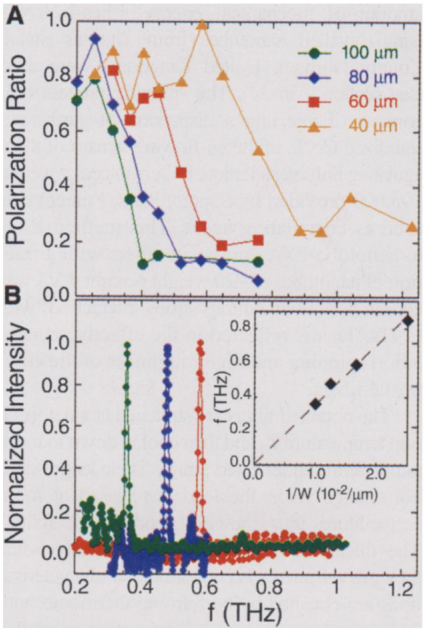

Figure 1.8: Spectral characterization of the radiation [Ozyuzer, 2007].

Figure 1.8 shows the spectral characterization of the radiation observed for mesas of various widths. Also in the figure is a plot of the frequency as a function of inverse width. The linear relationship suggests that the frequency of the radiation is indeed imposed by the cavity mode.

CHAPTER 2: LITERATURE REVIEW

The purpose of this literature review is two-fold. Firstly, to introduce and analyze in a systematic way the basic concepts of electromagnetic theory that are required in calculating radiation patterns from sources. Secondly, to provide a detailed overview of previous work on the subject and to generalize the approach taken so that it can be applied in other related circumstances.

The time-averaged power radiated per unit solid angle of cylindrical and rectangular mesas has been worked out by Dr. Richard Klemm and Kazuo Kadowaki [Klemm and Kadowaki, 2010]. Here we assume that there are two radiation sources within the mesas, the primary uniform mode and the secondary non-uniform mode. In general, to find the primary source, one needs to determine the surface electric current density and use it to calculate the magnetic vector potential. The surface electric current density can be found by first determining the current within the mesa and then analyzing how this current is distributed in the mesa. For most mesas, the current within the sample may be assumed to have a general form, leaving only the geometric distribution to be analyzed. Once the magnetic vector potential is found, determining the radiation pattern becomes a straight forward procedure.

Radiation Integrals and Auxiliary Potential Functions

In radiation problems, the general goal is to determine the $\boldsymbol{E}$ (electric) and $\boldsymbol{H}$ (magnetic) fields generated by a source and the subsequent emitted power distribution [Balanis, 2005]. In the analysis of radiation problems, it is a very common practice to introduce auxiliary functions, known as *vector potentials*, to simplify the solution to the problems. The relevant vector potential functions in this thesis are $\boldsymbol{A}$ (the magnetic vector potential) and $\boldsymbol{F}$ (the electric vector potential). To deter-

mine the $\boldsymbol{E}$ and $\boldsymbol{H}$ fields, the general procedure is to find the auxiliary potential functions first and then determine the $\boldsymbol{E}$ and $\boldsymbol{H}$ fields using the auxiliary potentials.

In superconducting mesas, the ac Josephson effect leads to both uniform and non-uniform currents within the mesas. The uniform current source $\boldsymbol{J}$ leads to an electric field $\boldsymbol{E}$ obtained from the magnetic vector potential $\boldsymbol{A}$. The secondary electromagnetic cavity magnetic current $\boldsymbol{M}_S$ is obtained from the cavity resonance with the non-uniform part of the ac Josephson displacement current, and leads to the electric vector potential $\boldsymbol{F}$.

For the uniform current source $\boldsymbol{J}$ the fields are given by $\boldsymbol{H}_A = \frac{1}{\mu}\boldsymbol{\nabla} \times \boldsymbol{A}$ and $\boldsymbol{E}_A = -\frac{\partial \boldsymbol{A}}{\partial t}$, where μ is the magnetic permeability constant. For the magnetic current source $\boldsymbol{M}_S$ the fields are given by $\boldsymbol{E}_F = -\frac{1}{\epsilon}\boldsymbol{\nabla} \times \boldsymbol{F}$ and $\boldsymbol{H}_F = -\frac{\partial \boldsymbol{F}}{\partial t}$ where the subcripts A and F indicate that the fields are due to $\boldsymbol{A}$ and $\boldsymbol{F}$ respectively and ϵ is the dielectric constant. In addition, the total fields may be obtained through the use of Schelkunoff's procedure of adding the electric and magnetic fields such that $\boldsymbol{E} = \boldsymbol{E}_A + \boldsymbol{E}_F$ and $\boldsymbol{H} = \boldsymbol{H}_A + \boldsymbol{H}_F$. Therefore, we may calculate each source separately and add them at the end.

Taking the source coordinates to be primed $\boldsymbol{x}'$ coordinates and the unprimed detector coordinates $\boldsymbol{x}$, the magnetic and vector potentials are given by

$$\boldsymbol{A}(\boldsymbol{x}, t) = \frac{\mu_0}{4\pi}\int d^3\boldsymbol{x}'\boldsymbol{J}(\boldsymbol{x}', t)\frac{e^{ikR}}{R}, \quad \boldsymbol{F}(\boldsymbol{x}, t) = \frac{\epsilon_0}{4\pi}\int d^3\boldsymbol{x}'\boldsymbol{M}_s(\boldsymbol{x}', t)\frac{e^{ikR}}{R}, \tag{2.1}$$

where $R = |\boldsymbol{x} - \boldsymbol{x}'|$. According to the far-field approximation we may write $\frac{e^{ikR}}{R} \rightarrow \frac{e^{ikr}}{r}e^{-i\boldsymbol{k}\cdot\boldsymbol{x}'}$. Finally, the time-averaged power radiated per unit solid angle is given by [Balanis, 2005]

$$\frac{dP}{d\Omega} = \frac{1}{2}\text{Re}[r^2\hat{\boldsymbol{r}} \cdot \boldsymbol{E} \times \boldsymbol{H}^*] \tag{2.2}$$

In the superconducting mesas used in the experiments, the electric field $\boldsymbol{E}$ and electric current density $\boldsymbol{J}$ are both in the $\hat{z}$ direction. This implies that the current is parallel to the boundary of the sample. Hence, we want the transverse magnetic (TM) modes, and that requires the magnetic field to be transverse to the boundary. We thus require that the tangential component of the magnetic field parallel at the boundary vanishes, i.e. we require $\boldsymbol{H}^{||}(\boldsymbol{x}'t)\Big|_S = 0$.

The most straight forward and simple way to implement the boundary conditions is by using *Love's Equivalency Principle*. As pictured in figure 2.1, we draw a surface around the regions of electric and magnetic fields $\boldsymbol{E}$ and $\boldsymbol{H}$, and place them with electric and magnetic surface currents $\boldsymbol{J}$ and $\boldsymbol{M}$. An equivalent picture of this system is obtained by placing the original fields outside and replacing them inside with arbitrary fields. The currents are then placed at the boundary of the surface. Because the fields inside are arbitrary we let them be equal to zero such that

$$\boldsymbol{J}(\boldsymbol{x}', t) = \hat{n} \times \boldsymbol{H}(\boldsymbol{x}', t)\Big|_S, \quad \boldsymbol{M}(\boldsymbol{x}', t) = \hat{n} \times \boldsymbol{E}(\boldsymbol{x}', t)\Big|_S \tag{2.3}$$

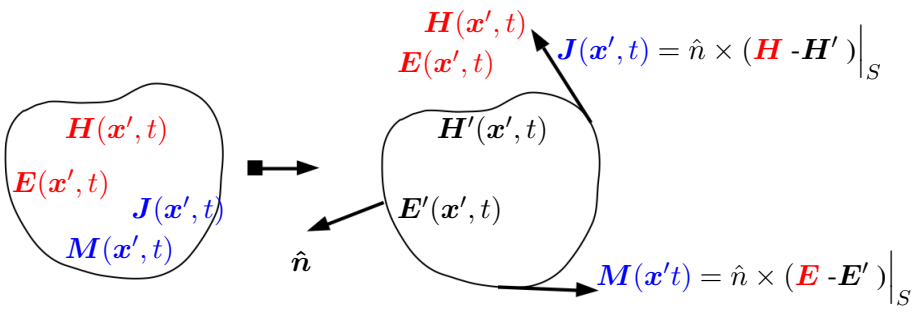

Figure 2.1: Illustration of Love's Equivalency Principle

Superconducting Mesa Radiation Theory

The superconductor BSCCO behaves as a stack of intrinsic Josephson junctions (IJJs). In BSCCO each of the junctions is naturally identical, as they are evenly spaced with two junctions per unit cell. By applying a static (dc) voltage V_0 across the mesa, the ac Josephson effect is generated in each of the N junctions involved in the mesa. The natural angular frequency of the Josephson current [Klemm and Kadowaki, 2010], as dictated by the ac Josephson relation within the mesa, is given by

$$\omega_J = \frac{2eV_0}{\hbar N} \tag{2.4}$$

The intrinsic nonlinearity of the Josephson junctions causes the ac Josephson current to have a large number of harmonics at $\nu_n = n\nu_J$, where $\nu_J = \omega_J/(2\pi)$, and ω_J is given by equation 2.4 [Klemm and Kadowaki, 2010]. We write the wave vector as $k_n = nk_J$. For simplicity, one may assume that during emission, all or most of the N junctions have synchronized and radiate together, so one may neglect the layer index of the spatial variation. Within the mesa we may write [Klemm and Kadowaki, 2010]

$$\boldsymbol{J}(\boldsymbol{x}', t) = \hat{z}' \sum_{n=1}^{\infty} e^{-in\omega_J t}[J_n^J + \delta J_n(\boldsymbol{x}')] \tag{2.5}$$

The uniform part of equation 2.5, i.e. J_n^J, is the main radiation source in superconducting mesas and will be used to calculate the uniform radiated power. The non-uniform radiated power is due to the non-uniform current $\delta J_n(\boldsymbol{x}')$, however, the spatial average of $\delta J_n(\boldsymbol{x}')$ vanishes and it's assumed that any time dependence is slow with respect to the measurement times and can be neglected [Klemm and Kadowaki, 2010].

Uniform Sources

In calculating the primary source, one may assume that the current source within the mesa is given by the uniform part of 2.5, i.e. one neglects $\delta J_n(\boldsymbol{x}')$ for the primary source to have

$$\boldsymbol{J}(\boldsymbol{x}', t) = \hat{z}' \sum_{n=1}^{\infty} e^{-in\omega_J t} J_n^J \tag{2.6}$$

Cavity Mode Sources

The non-uniform part $\delta J_n(\boldsymbol{x}')$ of the ac Josephson current provides the coupling to the electric field. Such non-uniformity can be due to defects and thermal fluctuations, which may be enhanced by inhomogeneous heating effects. In this thesis it's assumed that the non-uniformity is due to purely thermodynamic fluctuations [Klemm and Kadowaki, 2010].

Assuming $\left[\left\langle(\delta J_n)^2\right\rangle\right]^{1/2} << J_n^J$, the Helmholtz free energy of these fluctuations may be written as

$$\mathcal{F}_f \propto \sum_{n=1}^{\infty} \int d^2\boldsymbol{r}'[(\delta J_n)^2 + (\xi_n')^2(\boldsymbol{\nabla}\delta J_n)^2] \tag{2.7}$$

where $\xi(T)$ is a temperature-dependent characteristic length over which the spatial fluctuations in δJ_n occur, and n describes the intralayer spatial variations associated with the nth harmonic of the ac Josephson frequency. $\mathcal{F}_f$ is a minimum when $\frac{\partial \mathcal{F}_f}{\partial(\delta J_n)} = 0$, i.e.

$$-(\xi_n')^2(\boldsymbol{\nabla}')^2\delta J_n + \delta J_n = 0 \tag{2.8}$$

To find the resonant cavity radiation, equation 2.8 must be solved for δJ_n in the appropriate coordinate system and the respective boundary conditions of the geometry must be imposed. Once the form of δJ_n is known, one then proceeds to solve

$$\nabla^2 \boldsymbol{A}_r - \mu\epsilon \frac{\partial^2 \boldsymbol{A}_r}{\partial t^2} = -\mu \boldsymbol{J} \tag{2.9}$$

for $\boldsymbol{A}_r$. Finally, the secondary electromagnetic current $\boldsymbol{M}_s$ may be found using equation 2.3 through the relationship $\boldsymbol{M}_s = -\hat{\boldsymbol{n}} \times \boldsymbol{E}$ and the electric vector potential is given by equation 2.1.

Cylindrical Mesa

Assuming that no radiation emanates from the top and bottom of the mesa, the surface electric current density may be written inside the cylindrical mesa edge as

$$\boldsymbol{J}_S(\boldsymbol{x}', t) = \frac{a}{2}\eta(z')\delta(\rho' - a)\boldsymbol{J}(\boldsymbol{x}', t), \tag{2.10}$$

where for $h/a << 1$ it suffices to take $\eta(z') \rightarrow h\delta(z')$ and $\boldsymbol{J}(\boldsymbol{x}', t)$ is given by equation 2.6. Using the surface electric current density in the far-field approximation regime in equation 2.1, the magnetic vector potential $\boldsymbol{A}(\boldsymbol{x}, t)$ is given by

$$
\begin{aligned}
\boldsymbol{A}(\boldsymbol{x},t) &= \frac{a\mu_0}{8\pi}\int d^3\boldsymbol{x}'\sum_{n=1}^{\infty}\hat{z}'h\delta(z')\delta(\rho'-a)\frac{e^{ink_Jr}}{r}e^{-i\boldsymbol{k}\cdot\boldsymbol{x}'}e^{-in\omega_Jt}J_n^J \\
&= \frac{a\mu_0}{8\pi}\sum_{n=1}^{\infty}\frac{e^{ink_Jr}}{r}e^{-in\omega_Jt}J_n^J\int_0^a\rho'd\rho'\int_0^h dz'\int_0^{2\pi}d\phi'\hat{z}'\delta(z')\delta(\rho'-a)e^{-ink_J\rho'\sin\theta\cos(\phi-\phi')} \\
&= -\frac{a^2h\mu_0}{8\pi}\hat{\theta}\sin\theta\sum_{n=1}^{\infty}\frac{e^{ink_Jr}}{r}e^{-in\omega_Jt}J_n^J\int_0^{2\pi}d\phi' e^{-ink_Ja\sin\theta\cos(\phi-\phi')},
\end{aligned}
$$

where $\boldsymbol{k}\cdot\boldsymbol{x}' = k\rho'\sin\theta\cos(\phi-\phi')$ and $\hat{z}' = -\hat{\theta}\sin\theta$. The integral can be readily evaluated by noting that $J_n(u) = \frac{i^{-n}}{2\pi}\int_0^{2\pi}e^{i(u\cos\alpha+n\alpha)}$. Making the substitution $u = nk_\theta$, where $k_\theta = k_Ja\sin\theta$, the magnetic vector potential is given by

$$
\boldsymbol{A}(\boldsymbol{x},t) = -\frac{v\mu_0}{4\pi}\hat{\theta}\sin\theta\sum_{n=1}^{\infty}\frac{e^{ink_Jr}}{r}e^{-in\omega_Jt}J_n^JJ_0(nk_\theta), \tag{2.11}
$$

where $v = \pi a^2h$ is the volume of the mesa. The electric field $\boldsymbol{E}_A = -\frac{\partial\boldsymbol{A}}{\partial t}$ is given by

$$
\boldsymbol{E}_A(\boldsymbol{x},t) = -\frac{i\hat{\theta}\sin\theta v\mu_0}{4\pi r}\sum_{n=1}^{\infty}e^{ink_Jr}e^{-in\omega_Jt}n\omega_JJ_n^JJ_0(nk_\theta) \tag{2.12}
$$

In the far field approximation the magnetic field $\boldsymbol{H}_A(\boldsymbol{x},t)\rightarrow -\frac{i\omega_n}{Z_0}\hat{r}\times\boldsymbol{A}$, where $Z_0 = \sqrt{\mu_0/\epsilon_0}$ is

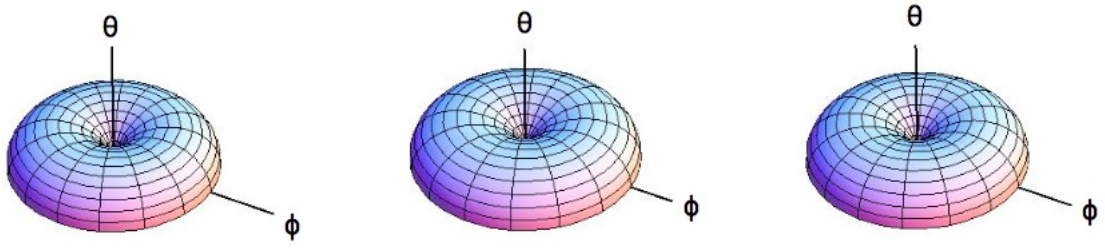

(a) (b) (c)

Figure 2.2: The three dimensional plots of the radiation in arbitrary units for cylindrical mesas from the uniform ac Josephson current alone, when the mesa is suspended in vacuum at the fundamental $n = 1$ frequency and modes (a) $(0, 1)$, (b) $(1, 1)$, and (c) $(2, 1)$.

the vacuum impedance [Balanis, 2005], therefore

$$\boldsymbol{H}_A(\boldsymbol{x}, t) = -\frac{i\hat{\phi}\sin\theta v\mu_0}{4\pi r Z_0}\sum_{n=1}^{\infty} e^{ink_J r}e^{-in\omega_J t}n\omega_J J_n^J J_0(nk_\theta) \tag{2.13}$$

As given by equation 2.2, the time-averaged power radiated per unit solid angle is given by

$$\frac{dP}{d\Omega} = \sin^2\theta\sum_{n=1}^{\infty}\left|B_n(\theta)J_0(nk_\theta)\right|^2, \tag{2.14}$$

where $B_n(\theta) = J_n^J vnk_J\sqrt{Z_0}/(4\sqrt{2}\pi)$ and we have used the relationship $\omega_J = k_J c$. The mode frequencies with the correct Love boundary condition $H_\phi(\rho' = a) = 0$ are given by $k'_{mp} = \chi'_{mp}/a$ inside the BSCCO mesa and $k'_{mp} = \chi'_{mp}/an_r$ outside the mesa.

The three-dimensional plots of $\mathcal{I}(\theta, \phi) \propto dP(\theta, \phi)/d\Omega$ in arbitrary units are then obtained. The

data are presented for the emission from the primary source, the ac Josephson current in the form of the surface electric current density J_S. In figure 2.2, the predicted $\mathcal{I}(\theta,\phi)$ is shown for the $n=1$ frequency with $k_J a = \chi_{01}/n_r, \chi_{11}/n_r$, and χ_{21}/n_r ac Josephson radiation, respectively for the mesa suspended in vacuum.

Rectangular Mesa Radiation Source

Once again, assuming that no radiation emanates from the top and bottom of the mesa, the surface electric current density may be written inside the rectangular mesa edges as

$$\boldsymbol{J}_S(\boldsymbol{x}',t) = \frac{1}{4}\eta(z')\boldsymbol{J}(\boldsymbol{x}',t)\sum_{\sigma=\pm}[f_\sigma(x',y')+g_\sigma(x',y')], \tag{2.15}$$

where $\boldsymbol{J}(\boldsymbol{x}',t)$ is given by equation 2.6, $f_\sigma(x',y') = w\delta(x'+\delta w/2)\Theta[(l/2)^2-(y')^2]$, and $g_\sigma(x',y') = l\delta(y'+\delta l/2)\Theta[(w/2)^2-(y')^2]$. For $h/w << 1$ and $h/l << 1$ it suffices to take $\eta(z') \to h\delta(z')$. Using the surface electric current density in the far-field approximation regime in equation 2.1, the magnetic vector potential $\boldsymbol{A}(\boldsymbol{x},t)$ is given by

$$\begin{aligned}\boldsymbol{A}(\boldsymbol{x},t) &= \frac{a\mu_0}{16\pi}\int d^3\boldsymbol{x}'\sum_{n=1}^{\infty}\hat{z}'h\delta(z')\frac{e^{ink_J r}}{r}e^{-i\boldsymbol{k}\cdot\boldsymbol{x}'}e^{-in\omega_J t}J_n^J\sum_{\sigma=\pm}[f_\sigma(x',y')+g_\sigma(x',y')]\\ &= \frac{a\mu_0}{16\pi r}\sum_{n=1}^{\infty}\hat{z}'e^{ink_J r}e^{-in\omega_J t}J_n^J\int_{-w/2}^{w/2}\int_{-l/2}^{l/2}\int_0^h h\delta(z')d^3\boldsymbol{x}'e^{-i\boldsymbol{k}\cdot\boldsymbol{x}'}\sum_{\sigma=\pm}[f_\sigma(x',y')+g_\sigma(x',y')]\end{aligned}$$

The integral is given by

$$
\begin{aligned}
I &= \int_{-w/2}^{w/2} dx' \int_{-l/2}^{l/2} dy' \big[f_+(x',y') + f_-(x',y')\big] e^{-ink_J \sin\theta(\cos\phi x' + \sin\phi y')} \\
&\quad + \int_{-w/2}^{w/2} dx' \int_{-l/2}^{l/2} dy' \big[g_+(x',y') + g_-(x',y')\big] e^{-ink_J \sin\theta(\cos\phi x' + \sin\phi y')} \\
&= w \int_{-w/2}^{w/2} dx' \int_{-l/2}^{l/2} dy' \Theta[(l/2)^2 - (y')^2] \big[\delta(x' + w/2) + \delta(x' - w/2)\big] e^{-ink_J \sin\theta(\cos\phi x' + \sin\phi y')} \\
&\quad + l \int_{-w/2}^{w/2} dx' \int_{-l/2}^{l/2} dy' \Theta[(w/2)^2 - (y')^2] \big[\delta(y' + l/2) + \delta(y' - l/2)\big] e^{-ink_J \sin\theta(\cos\phi x' + \sin\phi y')} \\
&= w(e^{-ink_J \sin\theta\cos\phi\frac{w}{2}} + e^{ink_J \sin\theta\cos\phi\frac{w}{2}}) \frac{(e^{-ink_J \sin\theta\sin\phi\frac{l}{2}} - e^{ink_J \sin\theta\sin\phi\frac{l}{2}})}{ink_J \sin\theta\sin\phi} \\
&\quad + l \frac{(e^{-ink_J \sin\theta\cos\phi\frac{w}{2}} - e^{ink_J \sin\theta\cos\phi\frac{w}{2}})}{ink_J \sin\theta\cos\phi} (e^{-ink_J \sin\theta\sin\phi\frac{l}{2}} + e^{ink_J \sin\theta\sin\phi\frac{l}{2}}) \\
&= 2wl\cos X_n \frac{\sin Y_n}{Y_n} + 2wl\cos Y_n \frac{\sin X_n}{X_n}
\end{aligned}
$$

where $X_n = (nk_J w/2)\sin\theta\cos\phi$ and $Y_n = (nk_J l/2)\sin\theta\sin\phi$. Altogether the magnetic vector potential is given by

$$
\boldsymbol{A}(\boldsymbol{x},t) = -\hat{\theta}\sin\theta \frac{v\mu_0}{8\pi r} \sum_{n=1}^{\infty} e^{ink_J r} e^{-in\omega_J t} J_n^J \chi_n, \tag{2.16}
$$

where $\chi_n = \cos X_n \frac{\sin Y_n}{Y_n} + \cos Y_n \frac{\sin X_n}{X_n}$ and $v = wlh$ is the volume of the mesa. The electric field $\boldsymbol{E}_A = -\frac{\partial \boldsymbol{A}}{\partial t}$ is given by

$$
\boldsymbol{E}_A(\boldsymbol{x},t) = i\hat{\theta}\sin\theta \frac{v\mu_0}{8\pi r} \sum_{n=1}^{\infty} e^{ink_J r} e^{-in\omega_J t} n\omega_J J_n^J \chi_n \tag{2.17}
$$

In the far field approximation the magnetic field $\boldsymbol{H}_A(\boldsymbol{x},t) \to -\frac{i\omega_n}{Z_0}\hat{r} \times \boldsymbol{A}$, where $Z_0 = \sqrt{\mu_0/\epsilon_0}$ is

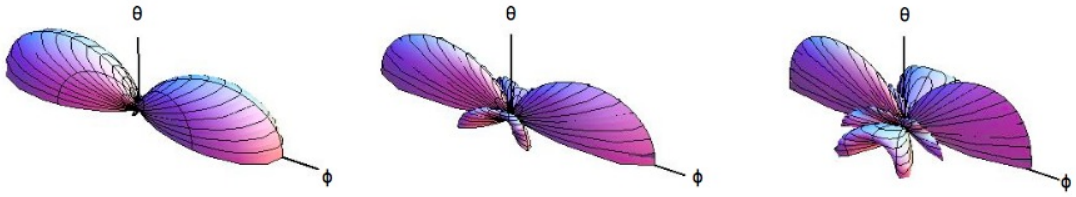

(a) (b) (c)

Figure 2.3: The three dimensional plots of the radiation in arbitrary units for rectangular mesas with $l/w = 20/3$ from the uniform ac Josephson current alone, when the mesa is suspended in vacuum. (a) At the fundamental $n = 1$ frequency with $k_1 w = \pi/n_r$. (b) At the second harmonic $n = 2$ with $k_2 w = 2\pi/n_r$. (c) At the third harmonic $n = 3$ with $k_3 w = 3\pi/n_r$.

the vacuum impedance [Balanis, 2005], therefore

$$\boldsymbol{H}_A(\boldsymbol{x}, t) = i\hat{\phi} \sin\theta \frac{v\mu_0}{\sqrt{Z_0} 8\pi r} \sum_{n=1}^{\infty} e^{ink_J r} e^{-in\omega_J t} n\omega_J J_n^J \chi_n \tag{2.18}$$

As given by equation 2.2, the time-averaged power radiated per unit solid angle is given by

$$\frac{dP}{d\Omega} = \frac{v^2 Z_0 k_J^2 \omega_J^2}{128\pi^2} \sum_{n}^{\infty} n^2 \Big| \sin\theta J_n^J \chi_n(\theta, \phi) \Big|^2 \tag{2.19}$$

The three-dimensional plots fo $\mathcal{I}(\theta, \phi) \propto dP(\theta, \phi)/d\Omega$ in arbitrary units are then obtained. The data are presented for the emission from the primary source, the ac Josephson current in the form of the surface electric current density J_S. In figure 2.3, the predicted $\mathcal{I}(\theta, \phi)$ is shown for the $n = 1$, $n = 2$, and $n = 3$ ac Josephson radiation, respectevely for the mesa suspended in vacuum.

Acute Isosceles Mesas

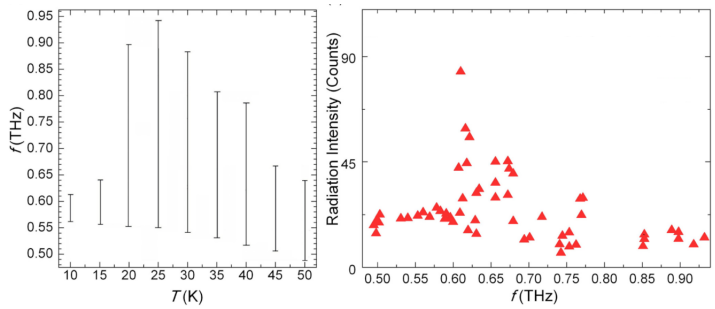

Figure 2.4: The bath temperature dependence of the measured emission frequencies and the overall emission intensity for T varying from 10.0 to 50.0 K [**?**]

Pictured in figure 2.4 is the frequency emission of an acute isosceles triangular mesas at various temperatures. From the figure we notice that as of the bath temperature T increases, the values and ranges (tunability) of the emission frequencies both decrease. In general, By changing both V and T the emission frequency can be tuned from 0.495 THz to 0.934 THz. One important characteristic of this figure is the apparent resonance at about 0.6 THz

Understanding the nature of this apparent resonance is very important because the wide tunability from 0.495 to 0.934 THz strongly suggests that acute triangular mesa shapes can greatly aid in the development of a useful device. At 0.61 THz, the estimated output power is 0.1 μW. While somewhat low, the tunability of the mesa allows for enhancement by placing the mesa in a tunable external EM cavity [**?**].

Our goal in the next section is to understand the nature of the cavity mode radiation enhancements and to calculate the expected radiation pattern from each of the modes.

CHAPTER 3: METHODOLOGY

The geometry dependence of the coherent THz radiation emitted from the intrinsic Josephson Junctions in mesas is of high interest, particularly for triangular mesas. Tunable radiation over the range from 0.495 to 0.934 THz was found to arise from an acute isosceles triangular mesa. This 47$\%$ tunability is the widest yet published from the outer current-voltage characteristic branch of such mesas of any geometry [**?**]

In calculating the time-averaged power radiated per unit solid angle of a pie-shaped wedge it's instrumental to follow the approach taken to solve the cylindrical and rectangular mesa radiation problem, and to compare the radiation sources as limiting cases whenever possible. The main difficulty in solving the radiation pattern of mesa sources is determining the geometric distribution of the current, particularly for triangular mesas.

Pie-Shaped Wedge Triangular Mesa Radiation Source

In the experiment by K. Delfanazari [**?**], the dimensions of the mesas (see table 3.1) were measured by an atomic force microscope.

Table 3.1: Sample bottom shape and T_c parameters of an acute isosceles triangular mesa

Mesa Shape	b (μm)	a (μm)	Thickness (μm)	$T_c(\Delta T_c)$ K
Isosceles	90	320	1.2	74.8 (1.3)

The current in the pie-shaped wedge mesa, as for any other mesa whose spatial variations can be ignored, is given by the homogeneous part of equation 2.6. The current distribution is not so easily determined and must be carefully studied. To do so, the magnetic vector potential resulting from

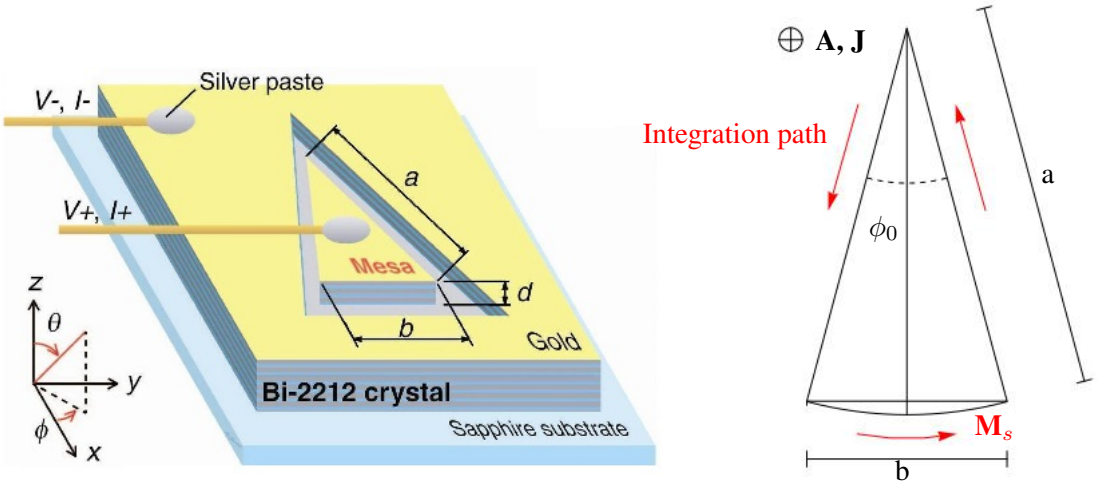

(a) (b)

Figure 3.1: An acute isosceles triangular mesa model. (a) A schematic view of an acute isosceles triangular mesa. Thin layers of Ag and Au are coated on the surface of the single crystal. Two gold wires are attached on both sides of the groove etched into the single crystal in order to apply current in the c-axis direction of BSCCO [**?**]. (b) Sketch of an acute isosceles triangular mesa and pie-shaped wedge model.

the assumed current distribution will be compared to the one obtained assuming a bulk average. The differences will be compared to those found in the work done on cylindrical and rectagular mesas. In general, the current distribution that best approximates the bulk average should be used.

A sketch of an acute isosceles triangular mesa is pictured in Fig. 3.1. The isosceles shape is to be approximated by the pie-shaped wedge model. The integration and $\boldsymbol{M}_s$ directions are indicated by the red arrows. The uniform ac Josephson current source $\boldsymbol{J}$ leads to the electric field $\boldsymbol{E}$ obtained from the magnetic vector potential $\boldsymbol{A}$, which are both in the z direction, normal to the plane, indicated in black. The electric vector potential $\boldsymbol{F}$ is in the direction of the magnetic current density source $\boldsymbol{M}_S(\boldsymbol{x}', t) = -\hat{\boldsymbol{n}} \times \boldsymbol{E}$.

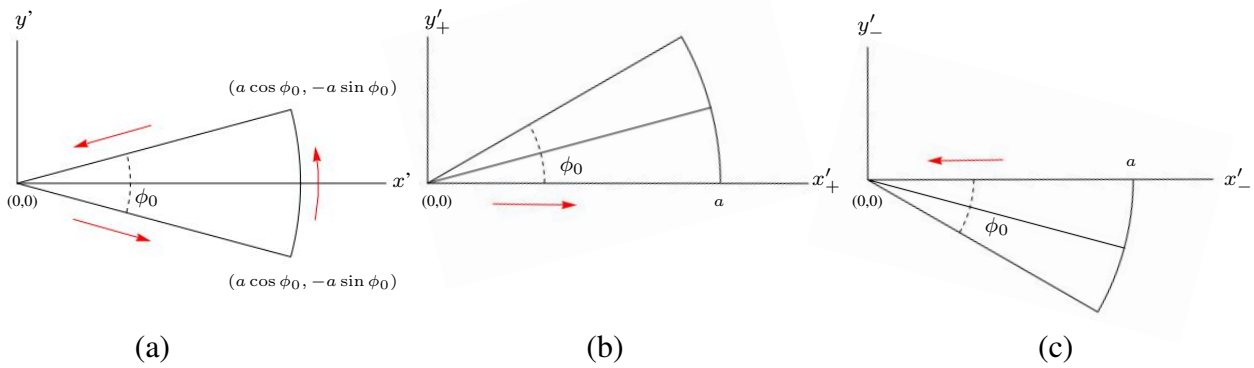

Figure 3.2: Sketch of a pie-shaped wedge in (a) standard cartesian coordinates, and (b),(c) rotated cartesian coordinates.

Primary

Depicted in figure 3.2a is the rectangular coordinate system that may be used in the integration. In this coordinate system the surface electric currenty density may be written as

$$\mathbf{J}_S(\mathbf{x}', t) = \eta(z')\varsigma(x', y')\mathbf{J}(\mathbf{x}', t), \tag{3.1}$$

where $\varsigma(x', y') = \frac{a}{2}\left[\Theta(\sqrt{x'^2 + y'^2} - a)\phi_0 \sum_{\sigma=\pm} \delta[y' + x'\sigma \tan\phi_0] + \delta[\sqrt{x'^2 + y'^2} - a]\Theta(\phi_0^2 - \phi'^2)\right]$ and **J**(**x**',t) is given by equation 2.6. Using the surface electric current density in the far-field approximation regime in equation 2.1, the magnetic vector potential $\mathbf{A}(\boldsymbol{x}, t)$ is given by

$$\mathbf{A}(\mathbf{x}', t) = \frac{\mu_0}{4\pi} \int dx'dy'dz'\mathbf{J}_S(\mathbf{x}', t)e^{-i(k_x x' + k_y y' + k_z z')} \frac{e^{ink_J r}}{r}, \tag{3.2}$$

where $k_x = nk_J \sin\theta\cos\phi_0$, $k_y = k_J \sin\theta\sin\phi_0$, and $k_z = k_J\cos\phi_0$. The integration can be simplified by using a rotated cartesian coordinates on the edges and polar coordinates on the arc. As illustrated in figures 3.2b and 3.2c, the pie-shaped wedge may be rotated by an angle $\pm\phi_0$ such that

$$x' = x'_{\pm}\cos\phi_0 \pm y'_{\pm}\sin\phi_0$$

$$y' = y'_{\pm}\cos\phi_0 \mp x'_{\pm}\sin\phi_0$$

Under this change of coordinates, $\delta[y + x\sigma\tan\phi_0]$ is logically equivalent to $\delta(y'_\sigma)$, therefore the magnetic vector potential becomes

$$\begin{aligned}
\mathbf{A}(\mathbf{x},t) &= \frac{\mu_0 a h\phi_0}{8\pi r}\int dx'_+ dy'_+ \delta(y'_+)\mathbf{J}(\mathbf{x}',t)e^{-i[k_x(x'_+\cos\phi_0 + y'_+\sin\phi_0) + k_y(y'_+\cos\phi_0 - x'_+\sin\phi_0) - nk_J r]} \\
&+ \frac{\mu_0 a h\phi_0}{8\pi r}\int dx'_- dy'_- \delta(y'_-)\mathbf{J}(\mathbf{x}',t)e^{-i[k_x(x'_-\cos\phi_0 - y'_-\sin\phi_0) + k_y(y'_-\cos\phi_0 + x'_-\sin\phi_0) - nk_J r]} \\
&+ \frac{\mu_0 a h}{8\pi r}\int \rho' d\rho' d\phi' \delta(\rho' - a)\mathbf{J}(\mathbf{x}',t)e^{-ink_J\rho'\sin\theta\cos(\phi-\phi')}e^{ink_J r} \\
&= \frac{\mu_0 a h\phi_0}{8\pi r}\int_0^a dx'_+ \mathbf{J}(\mathbf{x}',t)e^{-ink_J\sin\theta[x'_+\cos\phi\cos\phi_0 - x'_+\sin\phi_0\sin\phi_0]}e^{ink_J r} \\
&+ \frac{\mu_0 a h\phi_0}{8\pi r}\int_a^0 dx'_- \mathbf{J}(\mathbf{x}',t)e^{-ink_J\sin\theta[x'_-\cos\phi\cos\phi_0 + x'_-\sin\phi\sin\phi_0]}e^{ink_J r} \\
&+ \frac{\mu_0 a h}{8\pi r}\int_{-\phi_0}^{\phi_0} \rho' d\rho' d\phi' \delta(\rho' - a)\mathbf{J}(\mathbf{x}',t)e^{-ink_J\rho'\sin\theta\cos(\phi-\phi')}e^{ink_J r} \\
&= \frac{\hat{z}'\mu_0 a h}{8\pi r}\sum_{n=1}^{\infty} e^{-in\omega_J t}J_n^J\Bigg[\phi_0\int_0^a dx'_+ e^{-ink_J x'_+\sin\theta\cos(\phi+\phi_0)} \\
&- \phi_0\int_0^a dx'_- e^{-ink_J x'_-\sin\theta\cos(\phi-\phi_0)} + a\int_{-\phi_0}^{\phi_0} d\phi' e^{-ink_J a\sin\theta\cos(\phi-\phi')}\Bigg]
\end{aligned}$$

Finally, the magnetic vector potential may be written as

$$\mathbf{A}(\mathbf{x},t) = -\hat{\theta}\sin\theta\frac{\mu_0 v}{8\pi r}\sum_{n=1}^{\infty} e^{in(k_J r - \omega_J t)}J_n^J\Bigg[\chi_\sigma(\theta,\phi) + g(\theta,\phi)\Bigg], \tag{3.3}$$

where $\chi_\sigma(\theta,\phi) = \sum_{\sigma=\pm} -\sigma \frac{(e^{-ink_J a\sin\theta\cos(\phi+\sigma\phi_0)}-1)}{ink_J a\sin\theta\cos(\phi+\sigma\phi_0)}$, $g(\theta,\phi) = \frac{1}{\phi_0}\int_{-\phi_0}^{\phi_0} d\phi' e^{-ink_J a\sin\theta\cos(\phi-\phi')}$ and $v = \phi_0 a^2 h$ is the volume of the mesa. The electric field $\mathbf{E}_A = -\frac{\partial \mathbf{A}}{\partial t}$ is given by

$$\mathbf{E}_A(\mathbf{x},t) = i\hat{\theta}\sin\theta\frac{\mu_0 v}{4\pi r}\sum_{n=1}^{\infty} e^{in(k_J r-\omega_J t)}e^{-ink_J h} n\omega_J J_n^J\Big[\chi_\sigma(\theta,\phi)+g(\theta,\phi)\Big], \tag{3.4}$$

In the far field approximation the magnetic field $\mathbf{H}(\boldsymbol{x},t) \to -\frac{i\omega_n}{Z_0}\hat{r}\times\mathbf{A}$, where $Z_0 = \sqrt{\mu_0/\epsilon_0}$ is the vacuum impedance, therefore

$$\mathbf{H}_A(\mathbf{x},t) = i\hat{\phi}\sin\theta\frac{\mu_0 v}{\sqrt{Z_0}4\pi r}\sum_{n=1}^{\infty} e^{in(k_J r-\omega_J t)}e^{-ink_J h} n\omega_J J_n^J\Big[\chi_\sigma(\theta,\phi)+g(\theta,\phi)\Big], \tag{3.5}$$

As given by equation 2.2, the time-averaged power radiated per unit solid angle is given by

$$\frac{dP}{d\Omega} = \frac{v^2 k_J^2 Z_0}{32\pi^2}\sum_n^{\infty} n^2\sin^2\theta\Big|J_n^J\big(\chi_\sigma(\theta,\phi)+g(\theta,\phi)\big)\Big|^2 \tag{3.6}$$

Cavity Mode

As described in Apendix B, this equation when written in cylindrical coordinates has even and odd solutions given by

$$\delta J_n^{(e)}(\rho',\phi) = \sum_m^{\infty} C_{\nu_m^{(e)}} J_{\nu_m^{(e)}}(k_n\rho')\cos[\nu_m^{(e)}\phi]$$
$$\delta J_n^{(o)}(\rho',\phi) = \sum_m^{\infty} C_{\nu_m^{(0)}} J_{\nu_m^{(o)}}(k_n\rho')\sin[\nu_m^{(o)}\phi]$$

where the even and odd modes are given by $\nu_m^{(e)} = \frac{m\pi}{\phi_0}$ and $\nu_m^{(o)} = \frac{(m+1/2)\pi}{\phi_0}$. δJ_n may be discontinuous at the boundary $\rho' = a$ therefore we assume the thermodynamic fluctuations are weak near the mesa edge and we take

$$\frac{\partial \delta J_n}{\partial \rho'}\Big|_{\rho'=a} = 0 \tag{3.7}$$

which leads to

$$\begin{aligned} \delta J_n^{(e)}(\rho', \phi) &= \sum_{m,p=1}^{\infty} C_{\nu_m^{(e)}} J_{\nu_m^{(e)}}(k_{mp}\rho') \cos[\nu_m^{(e)}\phi] \\ \delta J_n^{(o)}(\rho', \phi) &= \sum_{m,p=1}^{\infty} C_{\nu_m^{(0)}} J_{\nu_m^{(o)}}(k_{mp}\rho') \sin[\nu_m^{(o)}\phi] \end{aligned} \tag{3.8}$$

where $\chi_{mp} = k'_{mp}a$ is the pth non-vanishing value of equation 3.7 and $k'_{mp} = 1/\xi'_{mp}$.

Since the current density is directed along the z-axis (J_z), only an A_z component will exist, i.e. $\mathbf{A}_r(\boldsymbol{x}', t) = A_z(\boldsymbol{x}', t)\hat{z}'$ must satisfy

$$\nabla'^2 A_z - \mu\epsilon \frac{\partial^2 A_z}{\partial t^2} = -\mu \delta J_z(\boldsymbol{x}', t), \tag{3.9}$$

where $\delta J_z(\boldsymbol{x}', t)$ is given by equation 3.8 and the non-uniform part of equation 2.5, μ and ϵ are the magnetic permeability and dielectric constant inside the mesa, i.e. $n_r = \sqrt{\mu\epsilon}$. The differential

equation is satisfied by the particular solution

$$
\begin{aligned}
A_z^{(e)}(\boldsymbol{x}', t) &= \sum_{m=0;n,p=1}^{\infty} J_n^J e^{-in\omega_J t} C_{\nu_m^{(e)}} J_{\nu_m^{(e)}}(k_{mp}\rho') \cos[\nu_m^{(e)}\phi'] \\
A_z^{(o)}(\boldsymbol{x}', t) &= \sum_{m=0;n,p=1}^{\infty} J_n^J e^{-in\omega_J t} C_{\nu_m^{(0)}} J_{\nu_m^{(o)}}(k_{mp}\rho') \sin[\nu_m^{(o)}\phi']
\end{aligned}
\tag{3.10}
$$

The electric field is given by $\mathbf{E} = -\frac{\partial \mathbf{A}}{\partial t}$, while the magnetic current is given by $\mathbf{M}_S(\boldsymbol{x}', t) = -\hat{\mathbf{n}} \times \hat{\mathbf{E}}(\boldsymbol{x}', t)$, where $\hat{n} = \pm\hat{\phi}, \hat{\rho}$. As given by equation 2.1, the electric vector potential is given by

$$
\begin{aligned}
\mathbf{F}^{(e)}(\boldsymbol{x}, t) &= -\frac{\epsilon_0}{4\pi} \sum_{m=0;n,p=1}^{\infty} J_n^J e^{-in\omega_J t} \int d^3\mathbf{x}' \hat{n} \times \hat{z}' \eta(z') \varsigma(x', y') C_{\nu_m^{(e)}} J_{\nu_m^{(e)}}(k_{mp}^{(e)}\rho') \cos[\nu_m^{(e)}\phi'] \frac{e^{ikR}}{R} e^{-i\mathbf{k}\cdot\mathbf{x}} \\
\mathbf{F}^{(o)}(\boldsymbol{x}, t) &= -\frac{\epsilon_0}{4\pi} \sum_{m=0;n,p=1}^{\infty} J_n^J e^{-in\omega_J t} \int d^3\mathbf{x}' \hat{n} \times \hat{z}' \eta(z') \varsigma(x', y') C_{\nu_m^{(o)}} J_{\nu_m^{(o)}}(k_{mp}^{(o)}\rho') \sin[\nu_m^{(o)}\phi'] \frac{e^{ikR}}{R} e^{-i\mathbf{k}\cdot\mathbf{x}}
\end{aligned}
\tag{3.11}
$$

To find the radiated power due to the magnetic current from the electric potential the same approach is taken as with the magnetic vector potential. The power radiate per unit solid angle is thus given by

$$
\frac{dP_{\nu_n^{(e,o)}}}{d\Omega} \propto |F_{\nu_n^{(e,o)},\theta}|^2 \cos^2\theta + |F_{\nu_n^{(e,o)},\phi}|^2 \tag{3.12}
$$

CHAPTER 4: RESULTS

The analytic formula of the power radiated per unit solid angle in a pie-shaped wedge is given by formula 3.6 for the uniform source and by equation 3.12 for the non-uniform source. These equations are described by the corresponding eigenvalues, or cavity modes, and to each mode there is a specific resonant frequency.

The time-averaged power radiated by a pie-shaped wedge mesa per unit solid angle was calculated and plotted using the Mathematica code shown in appendix C. The radiation patterns shown below correspond to the radiation $\chi(m, \nu_0^{(e,o)})$ and frequency values are listed on table 4.1. Here we provide a brief account of the radiation patterns.

Table 4.1: Parameters for the Acute ϕ_0 angle: The lowest eigenvalues $\chi(m, \nu_n^{(o,e)})$ and the model frequencies $f_m^{(o,e)} = c_0\chi(m, \nu_n^{(o,e)})/(2n_r\pi a)$ calculated for $n_r = 4.2$.

m	$\chi(m, \nu_0^e)$	f(THz)	$\chi(m, \nu_0^o)$	f(THz)	$\chi(m, \nu_1^e)$	f(THz)
1	3.83	0.128	13.70	0.458	26.01	0.869
2	7.02	0.234	18.55	0.620	31.74	1.06
3	10.17	0.340	22.43	0.749		
4	13.32	0.445	26.04	0.870		
5	16.47	0.550	29.52	0.986		
6	19.62	0.655	32.92	1.10		
7	22.76	0.760				
8	25.90	0.866				
9	32.19	1.076				

Highlighted in red are those frequencies which seem to match those observed in experiments and who output intensity is the greatest. These plots are plotted below while the rest are provided in the appendix.

Pictured in figure 4.1 is isosceles mesa radiation frquency output taken at various temperatures.

The plot also shows the calculated TM modes at the top of the figure. Note that the minimum radiation observed is close to the first odd mode TM^o(1,0)=0.458 THz. The two subsequent odd modes are seen as peaks at TM^o(2,0)=0.620 THz and M^o(3,0)=0.749 THz. The second highest peak is in close agreement with the even mode TM^e(1,0)=0.655 THz. Also shown in figure 4.1 is a coordinate system to serve as a reference for the radiation plots.

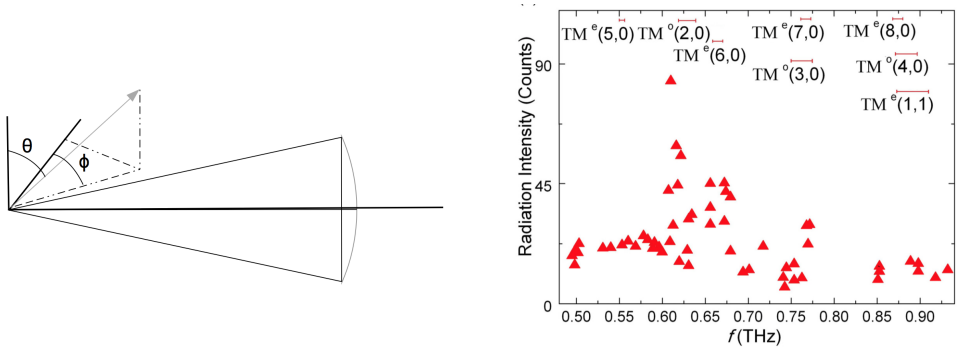

Figure 4.1: The bath temperature dependence of the measured emission frequencies and the overall emission intensity for T varying from 10.0 to 50.0 K [**?**] with some of the calculated TM modes at the top of the figure.

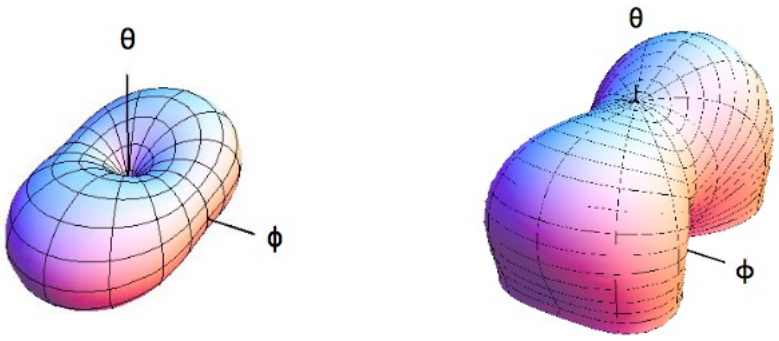

Figure 4.2: Uniform and cavity mode angular distributions for the mode TM^o(1,0)=0.458 THz

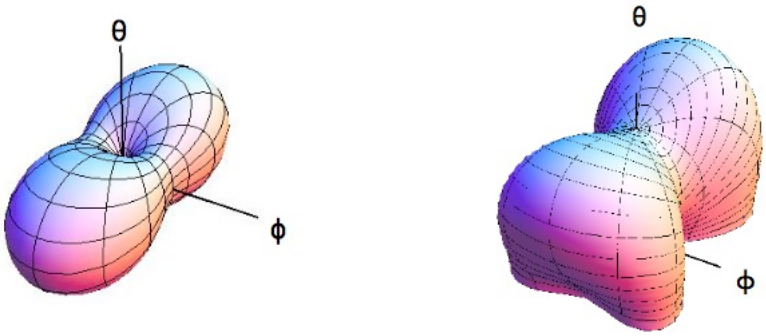

Figure 4.3: Uniform and cavity mode angular distributions for the mode TM^o(2,0)=0.620 THz

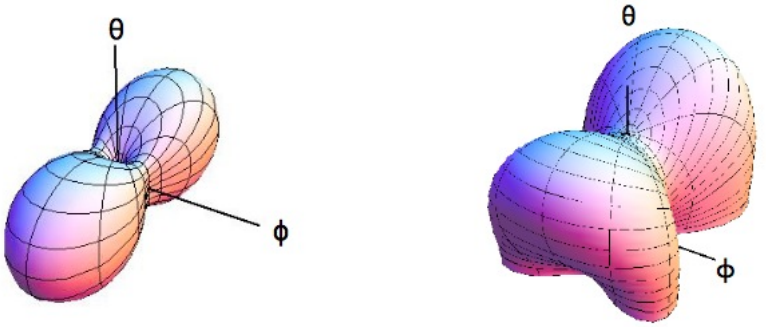

Figure 4.4: Uniform and cavity mode angular distributions for the mode TM^o(3,0)=0.749 THz

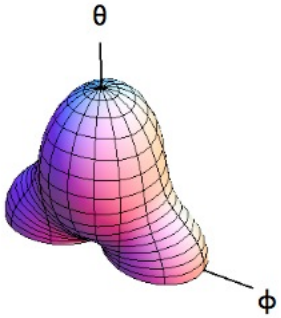

Figure 4.5: Cavity mode angular distributions for the mode TM^e(6,0)=0.655 THz

CHAPTER 5: CONCLUSION

The study of various mesa geometrical shapes is crucial for the understanding of the generation of cavity modes within the samples. In particular, triangular shapes such as the acute isosceles mesa play a significant role. We approximate the acute isosceles triangular mesa with a pie-shaped wedge geometry which is valid for all angles and results in a 1% difference for the values used by Delfanazari which are described as a $\phi_0 = 8^\circ$ angle.

To a large extend, the nature of the resonances observed in figure 2.4 have been accounted for as the peak frequency of the emission agrees well with a cavity resonance frequency of the isosceles triangular mesa. Furthermore, our results suggest that there are other resonant frequencies which have not yet been observed such as those in the lower even cavity modes. This could be due to temperature related effects. Nevertheless, our cavity mode frequencies are in general agreement with those observed in the emission spectrum of acute isosceles triangular mesas.

APPENDIX A: RADIATION PATTERNS

Uniform Source Modes

Uniform Even TM$^e(m,0)$ Modes

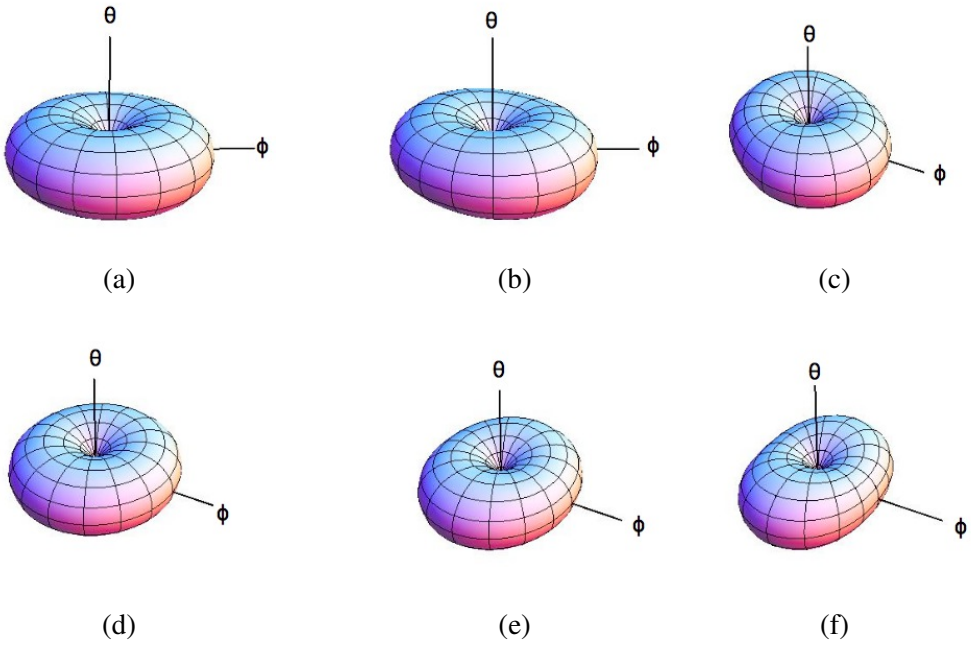

Figure A.1: Plots of the radiation intensity in arbitrary unites emitted from the uniform J_n^J part of the ac Josephson current when a pie-shaped wedge mesas is suspended in vacuum for the even modes $(m,0)$ using (a), (b), (c) the edge integration technique, and (d), (e), (f) the volume average integration technique. (a), (d) The mode (1,0), (b), (e) the mode (2,0), and (c), (f) the mode (3,0).

The radiation patterns expected with $k_J a = \chi_{10}/n_r \approx 3.8317/n_r$, $k_J a = \chi_{20}/n_r \approx 7.0156/n_r$, and $k_J a = \chi_{30}/n_r \approx 10.1735/n_r$ from the uniform part of the conducting dipole model when the mesa is suspended in vacuum are picture in figure A.1. Figures A.1a, A.1b, and A.1c represent the model obtained through the edge integration as picture in figure 3.1, while figures A.1d, A.1e, and A.1f represent the bulk average integration results. The radiation patterns resulting from the edge integration appear to be rotated by an angle ϕ_0, a feature which appears to be consistent for all the uniform radiation patterns obtained through the edge integration. In contrast to the radiation

patterns from the uniform part of a cylindrical mesa at $k_J a = \chi_{11}$ with $n = 1$ and $n = 2$, these radiation patterns are clearly distinguishable with most of the radiation perpendicular to the ϕ axis as the mode increases.

Uniform Even TM$^e(m, 1)$ Modes

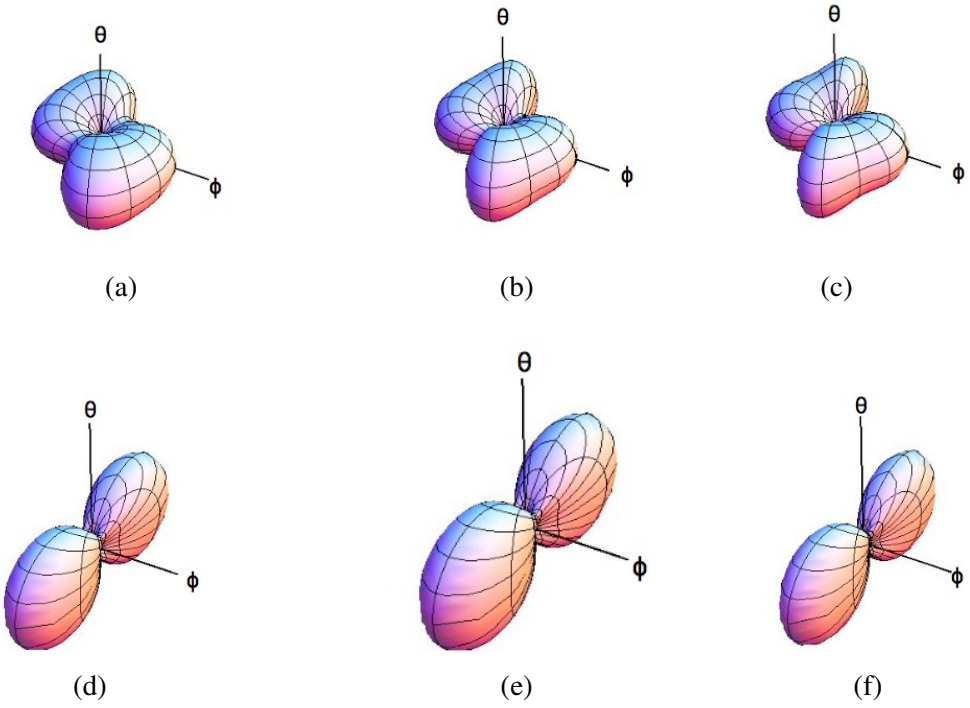

Figure A.2: Plots of the radiation intensity in arbitrary unites emitted from the uniform J_n^J part of the ac Josephson current when a pie-shaped wedge mesas is suspended in vacuum for the even modes $(m, 1)$ using (a), (b), (c) the edge integration technique, and (d), (e), (f) the volume average integration technique. (a), (d) The mode (1,0), (b), (e) the mode (2,0), and (c), (f) the mode (3,0).

The radiation patterns expected with $k_J a = \chi_{11}/n_r \approx 26.01/n_r$, $k_J a = \chi_{21}/n_r \approx 31.74/n_r$, and $k_J a = \chi_{31}/n_r \approx 36.16/n_r$ from the uniform part of the conducting dipole model when the mesa is suspended in vacuum are pictured in figure A.2. Figures A.2a, A.2b, and A.2c represent the model obtained through the edge integration as pictured in figure 3.1, while figures A.2d, A.2e, and A.2f

represent the bulk average integration results. Consistent with the previous results, the radiation patterns resulting from the edge integration appear to be rotated by an angle ϕ_0. Although the distortions in the radiation pattern appear to be consistent in both models, it appears that the model begins to deviate significantly from the bulk average at higher modes.

Uniform Odd TM$^o(m,0)$ Modes

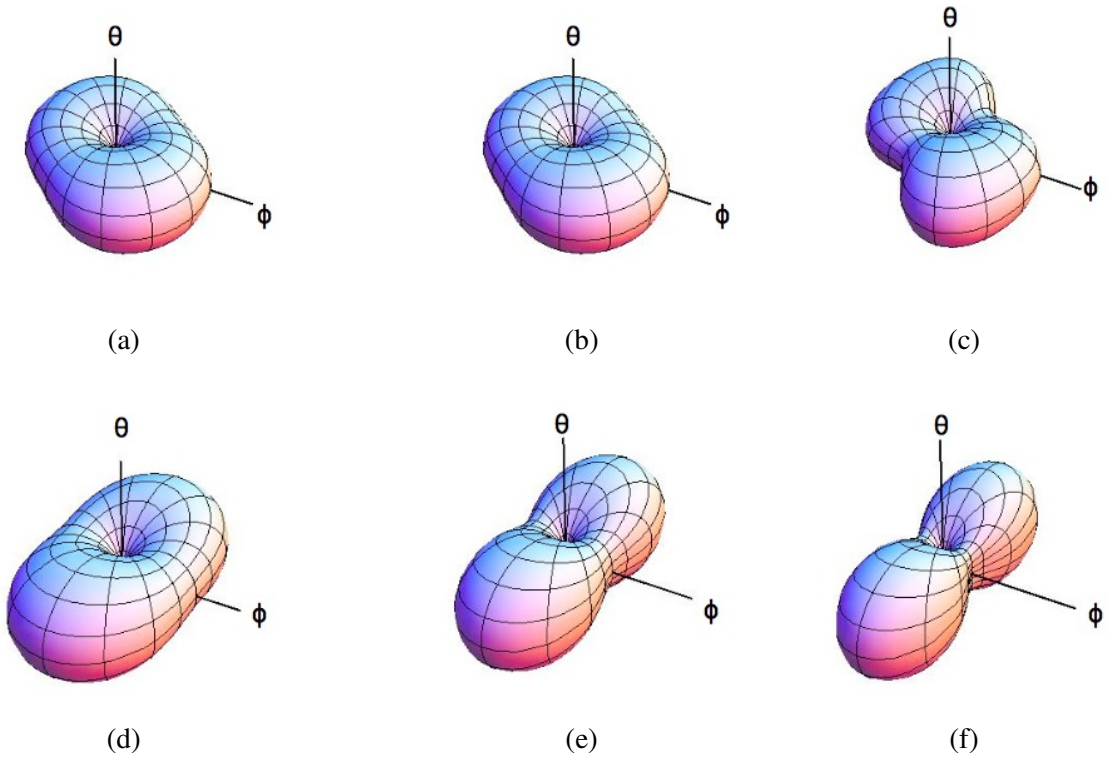

Figure A.3: Primary radiation patterns of a pie-shaped wedge mesa for the odd modes $(m,0)$ using (a), (b), (c) the edge integration technique, and (d), (e), (f) the volume average integration technique. (a), (d) The mode (1,0), (b), (e) the mode (2,0), and (c), (f) the mode (3,0).

The radiation patterns expected with $k_J a = \chi_{11}/n_r \approx 13.70/n_r$, $k_J a = \chi_{21}/n_r \approx 18.55/n_r$, and $k_J a = \chi_{31}/n_r \approx 22.43/n_r$ from the uniform part of the conducting dipole model when the mesa is suspended in vacuum are pictured in figure A.3. Figures A.3a, A.3b, and A.3c represent the model

obtained through the edge integration as pictured in figure 3.1, while figures A.3d, A.3e, and A.3f represent the bulk average integration results. In contrast to the even modes pictured in figure A.2, these odd modes appear to be more consistent with the bulk average. This is to be expected since the frequencies of these modes are lower than those pictured in figure A.2.

Non-Uniform Source Modes

Non-Uniform Even TM$^e(m,0)$ Modes

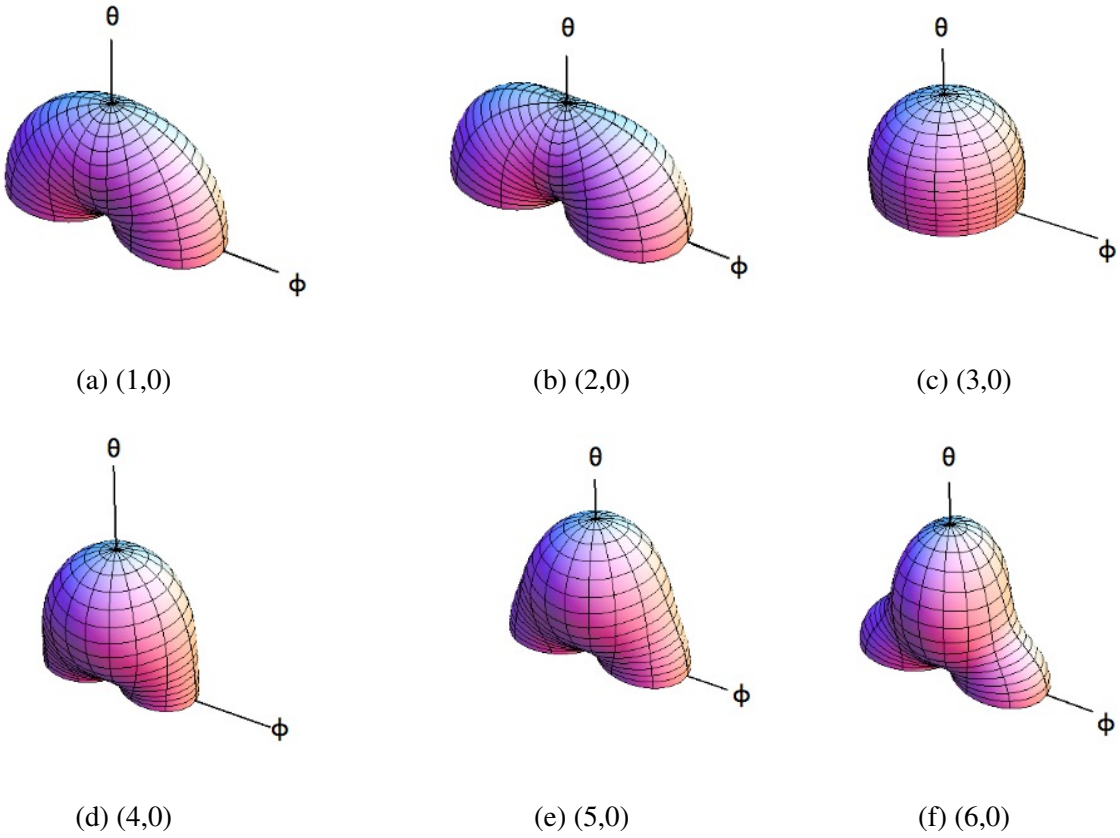

(a) (1,0) (b) (2,0) (c) (3,0)

(d) (4,0) (e) (5,0) (f) (6,0)

Figure A.4: Secondary radiation patterns of a pie-shaped wedge mesa for the even cavity modes $(m,0)$ with $m = 1-6$

In the radiation zone, spherical plots of the radiation intensity $\mathcal{I}(\theta,\phi)$ patterns for the TM cavity

modes with the lowest energies are shown for a pie-shaped wedge mesa suspended in vacuum in figures A.4, A.5, and A.6. The far-field radiation from the even cavity modes $(m, 0)$ with $m = 1-6$ are pictured in figure A.4 .

Non-Uniform Even TM$^e(m, 1)$ *Modes*

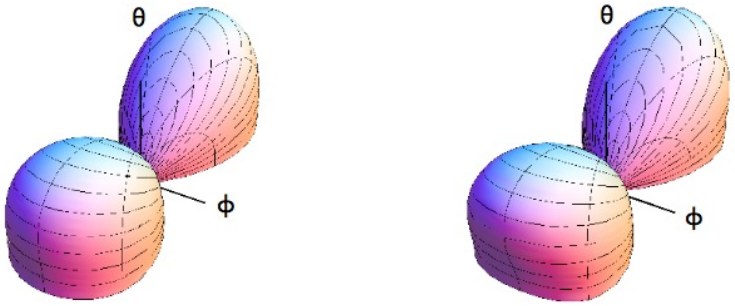

(a) (b)

Figure A.5: Primary radiation patterns of a pie-shaped wedge mesa for the even $(m, 1)$ modes with $m = 1, 2$ for the (a) (1,1) mode and (b) (2,1) mode.

The far-field radiation from the even cavity modes $(m, 0)$ with $m = 1 - 2$ are pictured in figure A.5.

Non-Uniform Odd TM$^o(m,0)$ Modes

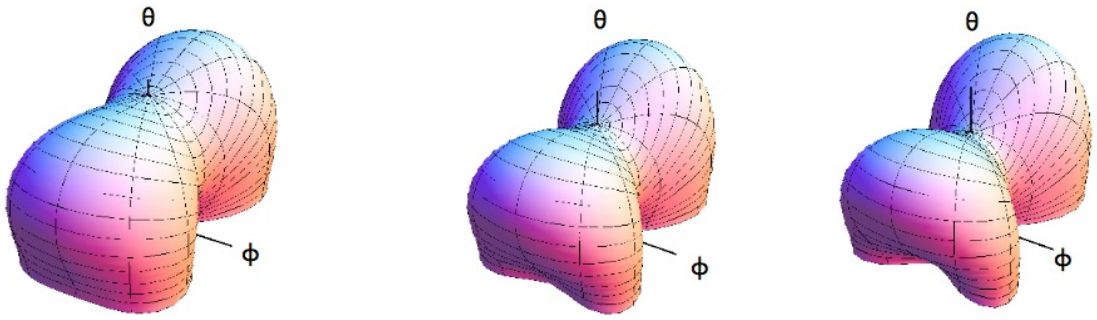

(a) (b) (c)

Figure A.6: Primary radiation patterns of a pie-shaped wedge mesa for the odd cavity modes $(m,0)$ with $m = 1-3$ for the (a) (1,0) mode, (b) (2,0) mode, and (c) (3,0) mode.

The far-field radiation from the odd cavity modes $(m,0)$ with $m = 1-3$ are pictured in figure A.6

APPENDIX B: HELMHOLTZ DIFFERENTIAL EQUATION

The non-uniform part $\delta J_n(\boldsymbol{x}')$ is found by solving the differential equation

$$\nabla^2 \delta J_n - \frac{1}{(\xi_n)^2}\delta J_n = 0$$

Letting $k_n = \frac{1}{\xi_n}$ the differential equation in polar coordinates is given by

$$\frac{1}{\rho}\frac{\partial}{\partial \rho}\Big(\rho \frac{\partial \delta J_n}{\partial \rho}\Big) + \frac{1}{\rho^2}\frac{\partial^2 \delta J_n}{\partial \phi^2} + k_n^2 \delta J_n = 0$$

Using separation of variables we write $\delta J_n(\rho, \phi) = R_n(\rho)\Phi_n(\phi)$. The equation reduces to

$$\frac{\rho^2}{R_n}\frac{d^2 R_n}{d\rho^2} + \frac{\rho}{R_n}\frac{dR_n}{d\rho} + k_n^2\rho^2 + \frac{1}{\Phi_n}\frac{d^2\Phi_n}{d\phi^2} = 0$$

The solution for Φ_n must be periodic and it can also be even or odd.

$$\Phi_n^{(e)}(\phi) = A_m^{(n)} \cos[\nu_m^{(e)}\phi]$$
$$\Phi_n^{(o)}(\phi) = B_m^{(n)} \sin[\nu_m^{(o)}\phi]$$

As part of Love's magnetic equivalence principle, the differential equation is subject to the condition $-\frac{1}{\mu}\frac{\partial A}{\partial \phi}\Big|_{\phi=\phi_0} = H_\phi\Big|_{\phi=\phi_0} = 0$, reducing the above functions to

$$\Phi_n^{(e)}(\phi) = C_{\nu_m^{(e)}} \cos[m\frac{\pi\phi}{\phi_0}]$$
$$\Phi_n^{(o)}(\phi) = C_{\nu_m^{(0)}} \sin[(m+\frac{1}{2})\frac{\pi\phi}{\phi_0}],$$

where the even and odd modes are given by $\nu_m^{(e)} = \frac{m\pi}{\phi_0}$ and $\nu_m^{(o)} = \frac{(m+1/2)\pi}{\phi_0}$. In this form, the differential equation reduces to

$$\frac{\rho^2}{R_n}\frac{d^2R_n}{d\rho^2} + \frac{\rho}{R_n}\frac{dR_n}{d\rho} + (k_n^2\rho^2 - (\nu_m^{(e,o)})^2) = 0$$

This is a Bessel differential equation with a solution given by

$$R_n(\rho) = C_m^{(n)} J_{\nu_m^{(e,o)}}(k_n\rho) + D_m^{(n)} Y_{\nu_m^{(e,o)}}(k_n\rho)$$

where $J_{\nu_m^{(e,o)}}(k_n\rho)$ and $Y_{\nu_m^{(e,o)}}(k_n\rho)$ are Bessel functions of the first and second kinds, respectively. In R_n the coefficient $D_m^{(n)}$ is set to zero because $Y_{\nu_m^{(e,o)}}$ diverges at $\rho = 0$. Taking into account the even and odd symmetry, the general solution to δJ_n is thus given by

$$\delta J_n(\rho,\phi) = \sum_m^{\infty} C_{\nu_m^{(e)}} J_{\nu_m^{(e)}}(k_n\rho)\cos[\frac{m\pi}{\phi_0}\phi]$$
$$\delta J_n(\rho,\phi) = \sum_m^{\infty} C_{\nu_m^{(0)}} J_{\nu_m^{(o)}}(k_n\rho)\sin[(m+\frac{1}{2})\frac{\pi\phi}{\phi_0}]$$

APPENDIX C: MATHEMATICA CODE

The time-averaged power radiated per unit solid angle was evaluated and plotted using two distinct approaches. One approach optimizes the computation time while the other optimizes the accuracy of the results and the quality of the plots. A combination of both methods was used throughout the development of this thesis and below is a highlight of the main characteristics of each.

To decrease the computation time we only evaluate the power function at certain angles. Suppose that the power distribution P is a function of θ, ϕ and perhaps some other constants such as the mode or index of refraction which we denote as $\alpha, \beta, ...$ First, a data set is created which contains the angles at which the function is to be evaluated:

$T_\theta = Table[\frac{\theta\pi}{180}, \{\theta, 0, 180, m\}]$,

$T_\phi = Table[\frac{\phi\pi}{180}, \{\theta, 0, 360, m\}]$,

$AngleData = Tuples[\{T_\theta, T_\phi\}]$,

where m determines the spacing between angles. Thus, a higher number will produce a larger set of angles, increasing the accuracy and quality of the graph but significantly increasing the computation time. Next, a separate function F is created which evaluates the angular dependent function P at a specific point (θ, ϕ) in such a way that the resulting data set includes the angle at which it was evaluated:

$FunctionName[\{\theta\_, \phi\_, \alpha\_, \beta\_, ...\}] := \{\{\theta, \phi\}, P(\theta, \phi, \alpha, \beta, ...)\}$

Finally, the data is mapped, interpolated and plotted:

$MappedData = Map[Functionname, AngleData]$,

$InterpolatedData = Interpolation[MappedData]$,

$PlotOfData = SphericalPlot3D[\{InterpolatedData[\theta, \phi], \{\theta, 0, \pi\}, \{\phi, 0, 2\pi\}, PlotRange \rightarrow$

$Full\}]$,

For cases in which a higher accuracy and quality is desired, we may define the function F directly by using $?NumericQ$, i.e.

$FunctionName[\{\theta\_?NumericQ, \phi\_?NumericQ, \alpha\_?NumericQ, ...\}] := P(\theta, \phi, \alpha, ...)$,

and simply plot the function using

$PlotOfData = Show[SphericalPlot3D[Norm[FunctionName[\theta, \phi]]],$
$\{\theta, 0, \pi\}, \{\phi, 0, 2\pi\}, PlotRange \to Full]$,

LIST OF REFERENCES

[Delfanazari et al., 2013] K. Delfanazari, H. Asai, M. Tsujimoto, T. Kashiwagi, T. Kitamura, T. Yamamoto, M. Sawamura, K. Ishida, C. Watanabe, S. Sekimoto, H. Minami, M. Tachiki, R. A. Klemm, T. Hattori, and K. Kadowaki, *Tunable terahertz emission from the intrinsic Josephson junctions in acute isosceles triangular $Bi_2Sr_2CaCu_2O_{8+\delta}$ mesas* Opt. Express **21**, 2171-2184 (2013)

[Armstrong, 2012] Carter M. Armstrong *The Truth About Terahertz: Anyone hoping to exploit this promising region of the electromagnetic spectrum must confront its very daunting physics.* L3 Communications, San Carlos, California, 2012.

[Orita et al., 2010] N. Orita, H. Minami, T. Koike, T. Yamamoto, and K. Kadowaki *Synchronized operation of two serially connected Bi2212 THz emitters*. Physica C470, S786S787 (2010).

[Bahl and Bhartiya, 1980] I. J. Bahl and P. Bhartiya *Microstrip Antennas*. (Artech House, 1980).

[Klemm and Kadowaki, 2010] Klemm R. and Kadowaki K., *Output from a Josephson stimulated terahertz amplified radiation emitter*. J. Phys.: Condens. Matter 22 (2010)

[Balanis, 2005] Balanis C A 2005 *Antenna Theory, Analysis and Design* 3rd edn (Hoboken, NJ: Wiley)

[Tinkham, 1975] Tinkham M 1975 *Introduction to Superconductivity* New York: McGraw-Hill, 1975. Print.

[Decker, 1969] Dekker M *Superconductivity* New York: M. Dekker, 1969. Print.

[Karpowickz, 2005] Nicholas Karpowicz et al *Comparison between pulsed terahertz time-domain imaging and continuous wave terahertz imaging* Semicond. Sci. Technol. 20 S293 (2005)

[Kashiwagi, 2014] T. Kashiwagi, K. Nakade, Y. Saiwai, H. Minami, T. Kitamura, C. Watanabe, K. Ishida, S. Sekimoto, K. Asanuma,T. Yasui, Y. Shibano, M. Tsujimoto, T. Yamamoto, B. Markovi, J. Mirkovi, R. A. Klemm, and K. Kadowaki *Computed tomography image using sub-terahertz waves generated from a high-Tc superconducting intrinsic Josephson junction oscillator* J. Appl. Phys 082603 (2014); doi: 10.1063/1.4866898

[Ozyuzer, 2007] L. Ozyuzer et al. (2007) *Emission of Coherent THz Radiation from Superconductors* SCIENCE Vol. 318, No. 5854 1291-1293